QSO DECOMPOSITION

Xuheng Ding[1,2], Tommaso Treu[2], John Silverman[5], Simon Birrer[3], Malte Schramm[2], Federica, Angelea
Draft version November 26, 2018

ABSTRACT

To be written. To be written.

Subject headings: galaxies: active — galaxies: evolution

1. INTRODUCTION

skeleton
1. The ML relation and why understand its evolution is important.
2. To understand this evolution, it is important to trace to high redshift. So, why it is difficult.
3. Introduce reference. Woo's. SS13, Treu's, Park79. In the theory, DeGraf...
4. This work, we introduces samples till redshift 1.7.

2. OBSERVATIONS AND DATA REDUCTION

In this section, we summarize the sample selection, observations, and data reduction of our sample.

2.1. *Sample selection*

We aim to study the relation between the BH masses ($\mathcal{M}_{\rm BH}$) and their host galaxy properties including luminosities ($L_{\rm host}$) and stellar mass to redshift at $z > 1$. For this propose, we focus on the broad-line (type-1) AGNs as provided by the X-ray coverage of COSMOS (Civano et al. 2016), (E)-CDFS-S (Lehmer et al. 2005; Xue et al. 2011), and SXDS (Ueda et al. 2008) fields. We select the broad-line AGNs at redshift region $1.2 < z < 1.7$ which cover a BH range $7.5 < \log\mathcal{M}_{\rm BH} < 8.5$. The Near IR spectra of AGNs are available from the survey of Subaru's Fiber Multi-Object Spectrograph (FMOS, Kimura et al. 2010; Schulze et al. 2018), a near-infrared (0.9-1.8 μm) spectrograph have with 400 apertures. The FMOS survey provides the best $\mathcal{M}_{\rm BH}$ estimates by $H\alpha$ and $H\beta$ lines out to $z \sim 1.7$ (Greene & Ho 2005; Matsuoka et al. 2013; Nobuta et al. 2012).

Our final sample is composed of 36 AGNs; 32 of them are new systems **(32+4?, the information of these four sample?)**. To compare with the samples in the literature, we adopt the samples from ... **The samples from H0licow7** For the calibration with the local relation, we introduce the well-defined 19 local AGN measurements (Bennert et al. 2010; Peterson

dxh@astro.ucla.edu
[1] School of Physics and Technology, Wuhan University, Wuhan 430072, China
[2] Department of Physics and Astronomy, University of California, Los Angeles, CA, 90095-1547, USA
[3] Heidelberg Institute for Theoretical Studies, Schloss-Wolfsbrunnenweg 35, D-69118 Heidelberg, Germany
[4] Department of Physics, University of California, Davis, CA 95616, USA
[5] Kavli IPMU (WPI), UTIAS, The University of Tokyo, Kashiwa, Chiba 277-8583, Japan

et al. 2004) which defines the zero-point. Table 1 list all the AGN systems analyzed in this work.

2.2. *Observation and reduction*

2.2.1. *HST image Observation*

The high spatial resolution of the host image is required for the decomposition of the nuclear/host emission and the accurate estimate of the stellar of the host stellar mass. All the new 32 AGN systems were observed with the HST/WFC3 infrared channel, as the HST program GO-15115, PI: John Silverman. We selected to use the filters F125W ($1.2 < z < 1.44$) and F140W ($1.44 < z < 1.7$) according to the redshift of the targets. This selection could ensure that the broad $H\alpha$ line ($4000\mathring{A}$) is not present in the bandpass which could contaminate the host emissions due to the broad wings of the PSF.

For the new 32 AGN systems, each target one has six separate exposures with $\sim 399s$ (i.e. total exposure time $\sim 2394s$). The six exposures for each dither image were combined by the ASTRODRIZZLE software package, with an output pixel scale of $0\rlap{.}''0642$ by setting `pixfrac` parameter of 0.8 and a `gaussian` kernel. The other four AGNs in our sample have been observed with WFC3 serendipitously (2 in COSMOS from Kartaltepe (PI); PID: 13657). The noise level maps of the imaging data are a requirement in the study. The origin of the noise in each pixel is stems from the read noise, background noise and Poisson noise by the astronomical sources themselves. To take them into account, we measure the read noise and background noise level directly from the empty regions of the data. We calculate the effective exposure time in each pixel based on the drizzled `WHT` array maps to infer the Poisson noise level. To accurately measure the photometry, we also adopt the PHOTUTILS to estimate the background light which could come from both the sky and the detector.

With 18/32 of our sample have rest-frame UV images by Scoville, et al. 2007 Images were taken through the wide ACS/F814W filter at four dither pointing with $507s$ exposures. The final image is drizzled to $0\rlap{.}''03$ pixel scale. Given the multi-band image for these systems, we are able to infer their host color and assess the contribution of both the young and old stellar population to the stellar mass budge citet Gallazzi+Bell 2009 which insures an accurate inference of rest-frame R-band luminosity by K-correction, stellar mass and star formation rate (SFR).

2.2.2. *AGN Emission Line*

The $\mathcal{M}_{BH}$ of type-1 AGNs can be inferred using the so-called virial method. The kinematics of the broad-line region trace the gravitational field of the central black hole, assuming the motion of the broad-line region (BLR) gas is virialised. In this scenario, the width of the emission-line provide the scale of the velocity, while the AGN continuum luminosity establish an empirical scale of the BLR size. The virial method builds on these reverberation mapping results and is directly calibrated to the $\mathcal{M}_{BH}$.

For our targets, the $H\alpha$ and $H\beta$ emission-line properties have been investigated by Schulze et al. (2018) using the multi-object spectrograph Subaru/FMOS. We referred to this paper for the details of continuum fitting and emission line modeling. Since the other compared AGNs in the literature used different calibrations of the virial method, we adopt the list of consistent recipes McGill et al. (2008), H0licow7 to cross-calibrate the $\mathcal{M}_{BH}$ for all the samples in order to avoid any systematic bias in Section 3.2.

3. ANALYSIS

3.1. *Surface Photometry*

3.1.1. *PSF library*

The knowledge of the PSF is crucial for this study, especially when the nuclear image is unresolved with light distributed as the point source. Moreover, the PSF in known to be vary according to their frame position and the intensity. Thus, we build a library of PSFs which we select the bright, isolated, unsaturated PSF stars across all the observed field. Thanks to the available multi-wavelength data (Laigle et al. 2016), we are able to know the positions of stars nearby the QSO field and thus select a proper position and orientation of the HST frame to cover as much PSFs stars as possible.

We claim that, by building this library, the assumption is that the overall PSFs herein indicates all the possible PSF shape for each QSO. Since two filter, i.e. F140W and F125W, are selected for different samples, we selected 74 and 34 PSFs for the samples observed by F140W and F125W, respectively.

In the next subsection, we carry out the QSO decomposition using each PSF. We rank their performance based on the goodness so that the final inference of the host properties are weighted from the top-rank PSFs.

3.1.2. *Surface Photometry modeling method*

We simultaneously fit the two-dimensional flux distribution of the center nuclear and the underling host galaxy. Following common practice, we assume the unresolved nuclear as a scaled PSF image, while the host galaxy as a Sérsic profile. Note that the actual morphologies of the host galaxies could be even more complicated (e.g. bulge+disk). However, the purpose of adopting the Sérsic model is a simplified a first-order approximation of the surface brightness distribution with a flexible parameterization which provides sufficient freedom to infer the host flux given the high redshift range of our sample. We fit the objects which close to the QSO as the another Sérsic model, to minimize the impact of their light.

We adopt the imaging modeling tool LENSTRONOMY (arXiv:1803.09746), to decompose the host and nuclear image. The LENSTRONOMY is a multi-purpose open-source gravitational lens modeling python package. The flexibility of this package enable us to turn off the lensing channel and carry out the decomposition. We have tested that the inference by LENSTRONOMY could have consistent result compared to GALFIT. Will talk more in this part.

For each QSO system, the final host properties is inferred in several steps. First, we fit the flux distribution using each PSFs in the library. Given the QSO imaging data, PSF and noise level, we are able to infer the posterior distribution in the parameter space and optimize the best-fit parameters with minimized residuals. In this step, we infer the best-fit parameters for each PSFs in the library and the corresponding χ^2 value[6]. In the second step, we rank the performance of each PSF based on the reduced χ^2 value and select the top-8 PSFs so as to weight for the inferred property. The weights for each PSF is calculated by:

$$w_i = exp\left(-\frac{(\chi_i^2 - \chi_{best}^2)}{2\alpha\chi_{best}^2}\right), \qquad (1)$$

where the α is the inflation parameter so that when $i = 8$:

$$\alpha\frac{\chi_{i=8}^2 - \chi_{best}^2}{2\chi_{best}^2} = 2 \qquad (2)$$

In figure, we demonstrate the optimized result of each system inferred by LENSTRONOMY. We also show the weighting process for an example system – CID1174 in Table 2.

Likewise, for the 18 systems with ACS/F184W images, we infer their host properties using the same approach. There are in total 174 star-like PSFs in the fitting library. We assumed the shape of the galaxy are consistent between the ACS and WFC3. Since the effects of dust extinction and contrast between the (blue) AGN and (red) host is more favorable in IR band, we believe the inferred information of the galaxy shape by IR band are superior to the one by UV band. Thus, while fitting the host flux at ACS band, we fix the R_{eff} and Sérsic n to the value by IR.

We list all the inference of the host galaxy properties in the Table.

3.1.3. *Host luminosity*

To be written: 1.K-correction to infer the rest frame R-band. * The galaxy template inferred by the joint fitting of the SED and the host flux ratio by us.

Having inferred the value of the rest-frame R-band magnitude, the luminosity is derived by $\log L_R/L_{R,\odot} = 0.4(M_{R,\odot} - M_R)$, where $M_{R,\odot} = 4.61$ (Blanton & Roweis 2007).

We summarized the homogenized R-band luminosities in Table?

3.2. *BH masses*

Our selected systems are broad-line (type-1) AGNs whose $\mathcal{M}_{BH}$ can be estimated from single-epoch spectroscopy using the so-called virial method FMOS (e.g. McLure 2002; Shen 2013). This estimation is achieved by the assumption that the empirical scaling size of the BLR and the line-of-sight velocity width can be inferred in turn continuum luminosity ($L_{\lambda_{line}}$) and emission line width (FWHM), respectively.

To avoid any systematic bias between our samples and the literature samples, we cross-calibrate the $\mathcal{M}_{BH}$ by adopting the self-consistent recipes as used by H0licow7, McGill et al. (2008). Overall, we adopt the following virial formalism for the $H\alpha$ and $H\beta$ emission line:

---

[6] The LENSTRONOMY enable one to infer also the parametric confidence interval. However, given a fixed PSF image, the $1 - \sigma$ region of each parameter are extremely narrow

$$\log\left(\frac{\mathcal{M}_{\mathrm{BH}}(H\beta)}{M_\odot}\right) = 6.882 + 0.518\log\left(\frac{\lambda L_{\lambda_{5100}}}{10^{44}\mathrm{erg\ s^{-1}}}\right)$$
$$+\ 2\log\left(\frac{\mathrm{FWHM}(5100)}{1000\ \mathrm{km\ s^{-1}}}\right), \qquad (3)$$

and

$$\log\left(\frac{\mathcal{M}_{\mathrm{BH}}(H\alpha)}{M_\odot}\right) = 6.459 + 0.55\log\left(\frac{\lambda L_{\mathrm{H}\alpha}}{10^{42}\mathrm{erg\ s^{-1}}}\right)$$
$$+\ 2\log\left(\frac{\mathrm{FWHM}(\mathrm{H}\alpha)}{1000\ \mathrm{km\ s^{-1}}}\right), \qquad (4)$$

With the self-consistent cross-calibration, we estimate the $\mathcal{M}_{\mathrm{BH}}$ by adopting the emission line properties measured by Schulze et al. (2018). For the system with both $H\alpha$ and $H\beta$ emission line information, we adopt the average $\mathcal{M}_{\mathrm{BH}}$ value by these two. We summarized the inference of the $\mathcal{M}_{\mathrm{BH}}$ together with the details on the emission line in Table.

4. RESULTS

4.1. *M-L relation*

4.1.1. *Stellar mass estimates*

stellar mass

4.2. *M-M$_*$ relation*

5. SUMMARY

We presented the study of the Mbh and host property's evolution to high redshift until 1.8.

ACKNOWLEDGMENTS

REFERENCES

Bennert, V. N., Treu, T., Woo, J., et al. 2010, ApJ, 708, 1507 2.1
Blanton, M. R., & Roweis, S. 2007, AJ, 133, 734 3.1.3
Civano, F., Marchesi, S., Comastri, A., et al. 2016, ApJ, 819, 62 2.1
Greene, J. E., & Ho, L. C. 2005, ApJ, 630, 122 2.1
Kimura, M., Maihara, T., Iwamuro, F., et al. 2010, PASJ, 62, 1135 2.1
Lehmer, B. D., Brandt, W. N., Alexander, D. M., et al. 2005, ApJS, 161, 21 2.1
Matsuoka, K., Silverman, J. D., Schramm, M., et al. 2013, ApJ, 771, 64 2.1

Nobuta, K., Akiyama, M., Ueda, Y., et al. 2012, ApJ, 761, 143 2.1
Peterson, B. M., Ferrarese, L., Gilbert, K. M., et al. 2004, The Astrophysical Journal, 613, 682 2.1
Schulze, A., Silverman, J. D., Kashino, D., et al. 2018, ArXiv e-prints, arXiv:1810.07445 2.1, 2.2.2, 3.2
Ueda, Y., Watson, M. G., Stewart, I. M., et al. 2008, ApJS, 179, 124 2.1
Xue, Y. Q., Luo, B., Brandt, W. N., et al. 2011, ApJS, 195, 10 2.1

TABLE 1
THE SAMPLE INFORMATION FOR THE 32 SYSTEMS.

Object ID (1)	z (2)	WFC3/Filter (3)	RA (4)	DEC (5)
COSMOS-CID1174	1.552	F140W*	150.2789	1.9595
COSMOS-CID1281	1.445	???	150.4160	2.5258
COSMOS-CID206	1.483	F140W	149.8371	2.0088
COSMOS-CID216	1.567	F140W*	149.7918	1.8729
COSMOS-CID237	1.618	F140W*	149.9916	1.7243
COSMOS-CID255	1.664	???*	150.1017	1.8483
COSMOS-CID3242	1.532	F140W	149.7113	2.1452
COSMOS-CID3570	1.244	F125W	149.6411	2.1076
COSMOS-CID452	1.407	F125W*	150.0045	2.2371
COSMOS-CID454	1.478	F140W*	149.8681	2.3307
COSMOS-CID50	1.239	F125W*	150.2080	2.0833
COSMOS-CID543	1.301	F125W*	150.4519	2.1448
COSMOS-CID597	1.272	???*	150.5262	2.2449
COSMOS-CID607	1.294	F125W*	150.6097	2.3231
COSMOS-CID70	1.667	F140W	150.4051	2.2701
COSMOS-LID1273	1.617	F140W	150.0565	1.6275
COSMOS-LID1538	1.527	F140W*	150.6215	2.1588
COSMOS-LID360	1.579	F140W*	150.1251	2.8617
COSMOS-XID2138	1.551	F140W*	149.7036	2.5781
COSMOS-XID2202	1.516	F140W*	150.6530	1.9969
COSMOS-XID2396	1.600	F140W*	149.4779	2.6425
CDFS-1	1.630	F140W*	52.8990	-27.8600
CDFS-229	1.326	F125W*	53.0680	-27.6580
CDFS-321	1.570	F140W*	53.0486	-27.6239
CDFS-724	1.337	F125W	53.2870	-27.6940
ECDFS-358	1.626	F140W	53.0850	-28.0370
SXDS-X1136	1.325	F125W	34.8925	-5.1498
SXDS-X50	1.411	F125W	34.0267	-5.0602
SXDS-X717	1.276	F125W	34.5400	-5.0334
SXDS-X735	1.447	F140W	34.5581	-4.8781
SXDS-X763	1.412	F125W	34.5849	-4.7864
SXDS-X969	1.585	F140W	34.7594	-5.4291

NOTE. — Column 1: Object field and ID. Column 2: Redshifts. Column 3: HST filter. The samples with marker * have the ACS/F814W.

TABLE 2
THE PROCESS OF WEIGHTING FOR COSMOS-CID1174

PSF rank (1)	total χ^2 (2)	weights w_i (3)	host flux (counts) (4)	host flux ratio (5)	$R_{\rm eff}$(arcsec) (6)	Sérsic n (7)
1	8646.711	1.000	99.102	41.9%	$0\rlap{.}''298$	1.932
2	8816.947	0.849	76.740	33.0%	$0\rlap{.}''365$	1.102
3	9304.841	0.530	128.618	54.7%	$0\rlap{.}''231$	2.780
4	9652.575	0.379	187.498	79.0%	$0\rlap{.}''116$	6.175
5	10018.324	0.267	75.061	32.3%	$0\rlap{.}''365$	1.226
6	10087.456	0.249	79.835	34.3%	$0\rlap{.}''358$	1.195
7	10457.811	0.174	108.580	46.4%	$0\rlap{.}''262$	2.190
8	10721.421	0.135	63.994	27.8%	$0\rlap{.}''406$	0.720
Weighted value			103.534 ± 34.267	44.0%±14.2%	$0\rlap{.}''296\pm0\rlap{.}''079$	2.173±1.500

NOTE. — The detailed information of the weights for the inference of CID1174. The inflation value α calculated by Eq. 2 is 16.671.

TABLE 3
THE SAMPLE INFORMATION FOR THE 32 SYSTEMS.

Target ID	Inference by WFC3					Inference by ACS		
	reduced χ^2	host flux ratio	R_{eff} ($''$)	Sérsic n	magnitude (AB system)	reduced χ^2	host flux ratio	magnitude (AB system)
(1)	(2)	(3)	(4)	(5)	(6)	(7)	(8)	(9)
CID1174	2.324	44.0%±14.2%	0.296±0.079	2.173±1.5	$21.415^{+0.436}_{-0.31}$	2.484074	11.7%±1.4%	$23.165^{+0.138}_{-0.122}$
CID1281	...	...	...	...	...	...	...	...
CID206	2.054	35.7%±24.1%	0.282±0.151	3.191±2.51	$21.81^{+1.247}_{-0.565}$	1.903449	7.7%±2.4%	$23.671^{+0.403}_{-0.293}$
CID216	1.514	93.9%±4.7%	0.251±0.063	6.159±1.205	$21.51^{+0.052}_{-0.049}$	1.424993	35.1%±1.5%	$23.446^{+0.053}_{-0.051}$
CID237	2.349	29.9%±6.3%	0.872±0.172	4.736±1.701	$21.279^{+0.26}_{-0.209}$	2.353571	3.2%±2.0%	$23.718^{+1.037}_{-0.52}$
CID255	...	...	...	...	...	...	...	...
CID3242	2.751	46.1%±12.7%	0.201±0.159	6.142±1.874	$21.161^{+0.35}_{-0.264}$	2.595594	4.8%±1.3%	$23.595^{+0.337}_{-0.257}$
CID3570	1.665	76.5%±1.6%	0.698±0.007	0.728±0.054	$21.164^{+0.021}_{-0.021}$	1.331913	85.6%±1.5%	$22.971^{+0.012}_{-0.012}$
CID452	1.684	75.4%±3.9%	0.365±0.015	1.402±0.175	$21.176^{+0.063}_{-0.06}$	1.451608	37.8%±0.7%	$22.732^{+0.022}_{-0.022}$
CID454	2.203	35.3%±2.1%	0.391±0.013	0.602±0.092	$21.212^{+0.067}_{-0.063}$	1.29101	9.2%±0.5%	$23.352^{+0.058}_{-0.055}$
CID50	5.576	16.8%±8.7%	0.152±0.102	3.371±2.154	$20.915^{+0.796}_{-0.545}$	4.940352	5.0%±3.3%	$22.504^{+1.145}_{-0.545}$
CID543	1.902	31.8%±10.0%	0.1±0.0	0.505±0.333	$21.95^{+0.405}_{-0.294}$	1.434799	5.2%±2.0%	$23.765^{+0.534}_{-0.357}$
CID597	...	...	...	...	...	...	...	...
CID607	1.692	43.6%±17.9%	0.206±0.087	3.418±1.097	$21.189^{+0.575}_{-0.374}$	2.590398	4.7%±1.8%	$23.566^{+0.511}_{-0.346}$
CID70	2.041	19.6%±5.1%	0.426±0.101	3.543±1.154	$21.865^{+0.323}_{-0.248}$	2.36054	2.3%±1.1%	$24.625^{+0.677}_{-0.414}$
LID1273	1.697	53.3%±9.1%	0.302±0.04	1.22±0.49	$20.939^{+0.211}_{-0.176}$	2.136592	6.4%±0.8%	$23.289^{+0.153}_{-0.134}$
LID1538	2.362	43.5%±7.8%	0.177±0.042	2.819±0.475	$21.251^{+0.221}_{-0.184}$	2.172992	7.5%±1.2%	$23.088^{+0.189}_{-0.161}$
LID360	3.918	17.9%±1.1%	0.629±0.018	0.672±0.04	$21.483^{+0.068}_{-0.04}$	4.913659	3.7%±0.5%	$23.254^{+0.172}_{-0.149}$
XID2138	1.597	39.7%±6.1%	0.49±0.035	1.293±0.437	$21.845^{+0.188}_{-0.16}$	2.73139	5.0%±1.3%	$23.898^{+0.313}_{-0.243}$
XID2202	3.23	33.3%±8.0%	0.1±0.001	3.957±1.017	$21.16^{+0.302}_{-0.236}$	3.851762	8.3%±1.9%	$22.592^{+0.286}_{-0.226}$
XID2396	3.669	23.9%±10.5%	0.584±0.085	0.772±1.36	$21.404^{+0.652}_{-0.404}$	5.346128	2.3%±0.5%	$23.364^{+0.243}_{-0.198}$
CDFS-1	1.358	54.4%±17.3%	0.158±0.077	4.574±1.387	$22.656^{+0.414}_{-0.299}$	...	...	...
CDFS-229	4.329	17.6%±2.1%	0.507±0.026	0.463±0.195	$21.568^{+0.144}_{-0.127}$	...	...	...
CDFS-321	3.998	24.5%±11.7%	0.378±0.122	2.26±2.007	$20.337^{+0.703}_{-0.423}$	...	...	...
CDFS-724	1.355	34.7%±14.6%	0.118±0.03	1.618±1.099	$23.695^{+0.582}_{-0.377}$	...	...	...
ECDFS-358	2.012	56.4%±13.5%	0.359±0.043	1.671±0.542	$21.34^{+0.302}_{-0.236}$	...	...	...
SXDS-X1136	1.937	40.5%±7.8%	0.101±0.003	1.986±0.483	$21.921^{+0.231}_{-0.19}$	...	...	...
SXDS-X50	1.423	42.4%±9.1%	0.184±0.041	1.755±0.655	$21.943^{+0.266}_{-0.214}$	...	...	...
SXDS-X717	1.426	61.4%±9.1%	0.264±0.066	5.58±1.421	$21.759^{+0.176}_{-0.151}$	...	...	...
SXDS-X735	2.203	32.4%±8.5%	0.22±0.057	2.027±1.012	$20.919^{+0.333}_{-0.254}$	...	...	...
SXDS-X763	2.376	6.0%±4.0%	0.694±0.532	2.394±0.796	$24.134^{+1.172}_{-0.55}$	...	...	...
SXDS-X969	1.613	29.0%±11.7%	0.115±0.026	2.149±1.147	$21.594^{+0.553}_{-0.365}$	...	...	...

NOTE. — Column 1: Object field and ID. Column 2: Redshifts. Column 3: HST filter. The samples with marker * have the ACS/F814W.

TABLE 4
THE INFERENCE OF THE $\mathcal{M}_{BH}$ FOR THE 32 SYSTEMS.

Target ID	using emission line $H\alpha$			using emission line $H\beta$		
	FWHM (km s^{-1})	$\lambda L_{H\alpha}$ (10^{42}erg s^{-1})	$\mathcal{M}_{BH}$ (M$_\odot$)	FWHM(5100) (km s^{-1})	$\lambda L_{\lambda 5100}$ (10^{44}erg s^{-1})	$\mathcal{M}_{BH}$ (M$_\odot$)
(1)	(2)	(3)	(4)	(5)	(6)	(7)
CID1174	1906.3037	43.43237	7.807	5898.264	44.76243	8.818
CID1281	1619.4891	43.23945	7.559	...	...	...
CID206	3333.5527	43.4776	8.317	...	...	...
CID216	2229.5232	42.84509	7.62	...	...	...
CID237	2112.3306	43.85546	8.129	...	...	...
CID255	1932.0933	43.9924	8.127	3709.241	45.37122	8.731
CID3242	2543.2202	43.83323	8.278	3774.503	45.09891	8.605
CID3570	1958.8551	43.16374	7.683	...	...	...
CID452	3457.8801	42.92298	8.044	3127.3306	44.63353	8.201
CID454	2824.2693	43.34466	8.1	...	...	...
CID50	2339.9104	43.93786	8.263	1938.5676	45.32766	8.145
CID543	2188.8447	43.57404	8.005	...	...	...
CID597	1656.3296	43.32955	7.629	...	...	...
CID607	3009.1816	43.67079	8.335	4241.526	44.78209	8.542
CID70	2480.4058	43.50531	8.076	3981.8574	45.1582	8.682
LID1273	3223.8484	43.61001	8.361	...	...	...
LID1538	2941.422	43.59594	8.274	...	...	...
LID360	2481.7253	43.88091	8.283	2868.8992	45.08676	8.36
XID2138	3185.8613	43.6148	8.354	2944.7766	44.80782	8.239
XID2202	2973.2378	43.56249	8.265	...	...	...
XID2396	2271.2617	44.06196	8.306	2657.8386	45.50467	8.51
CDFS-1	...	...	...	...	...	...
CDFS-229	...	...	...	...	...	...
CDFS-321	2441.93	43.92714	8.294	...	...	...
CDFS-724	...	...	...	...	...	...
ECDFS-358	2237.2314	43.39674	7.927	...	...	...
SXDS-X1136	2759.8953	43.43305	8.129	6761.222	44.71429	8.912
SXDS-X50	1816.672	43.421	7.759	...	...	...
SXDS-X717	2930.7417	43.04988	7.97	...	...	...
SXDS-X735	2702.0962	43.69804	8.256	3519.6052	45.07463	8.532
SXDS-X763	2961.1743	43.57321	8.267	4508.5146	44.51285	8.456
SXDS-X969	2296.0566	43.50066	8.006	1695.7146	45.05337	7.886

NOTE. — Column 1: Object field and ID. Column 2: Redshifts. Column 3: HST filter. The samples with marker * have the ACS/F814W.
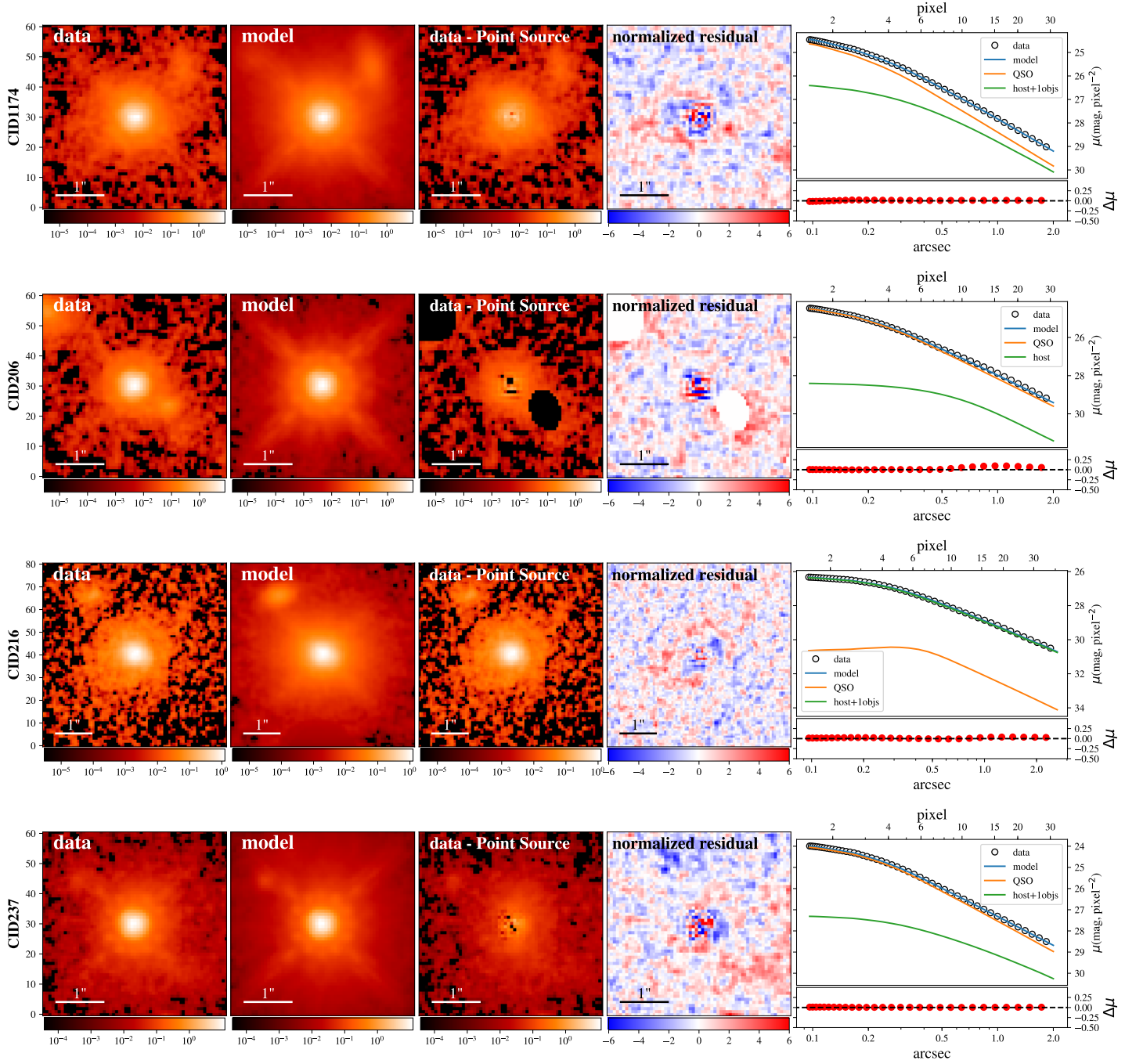
FIG. 1.— WFC3 F110W images for 12 objects. In each row, observed data (first column), best-fit models (second column), and residuals (third column) are presented with the object name. All images are $10.8'' \times 10.8''$ in size and displayed with an inverted asinh stretch. The fourth column shows the corresponding one-dimensional surface brightness profiles. In each top panel, the profiles measured from the data (open circles), the best-fit model (black solid line), and the sub-components of the model for bulge (blue solid line), disk (green solid line), AGN (red solid line) are shown. Residuals (gray circles), the difference of the profiles between the data and the best-fit model, are presented in each bottom panel. Note that the one-dimensional surface brightness profiles are shown for illustration purposes only, the actual fitting made use of the full two-dimensional images.
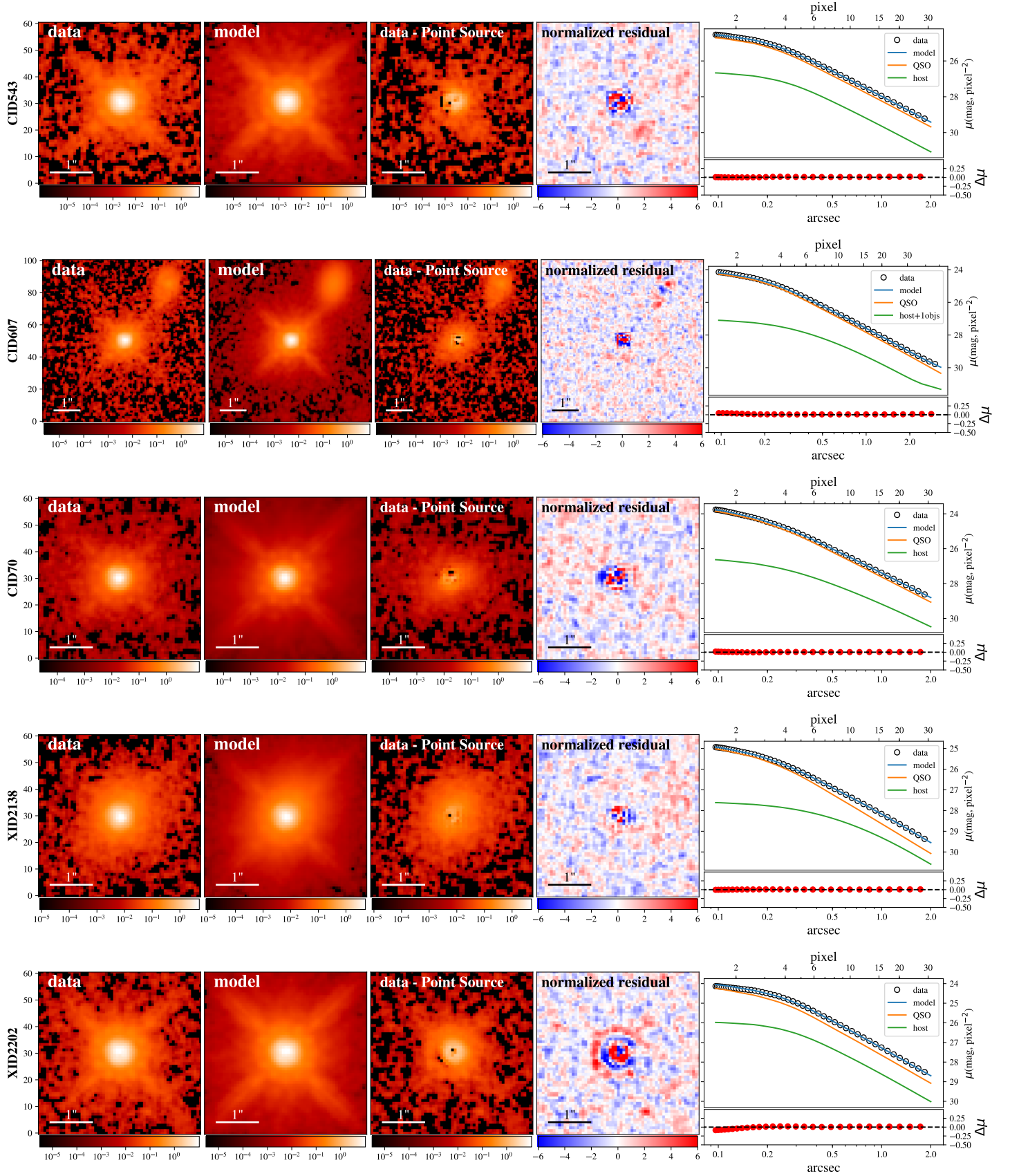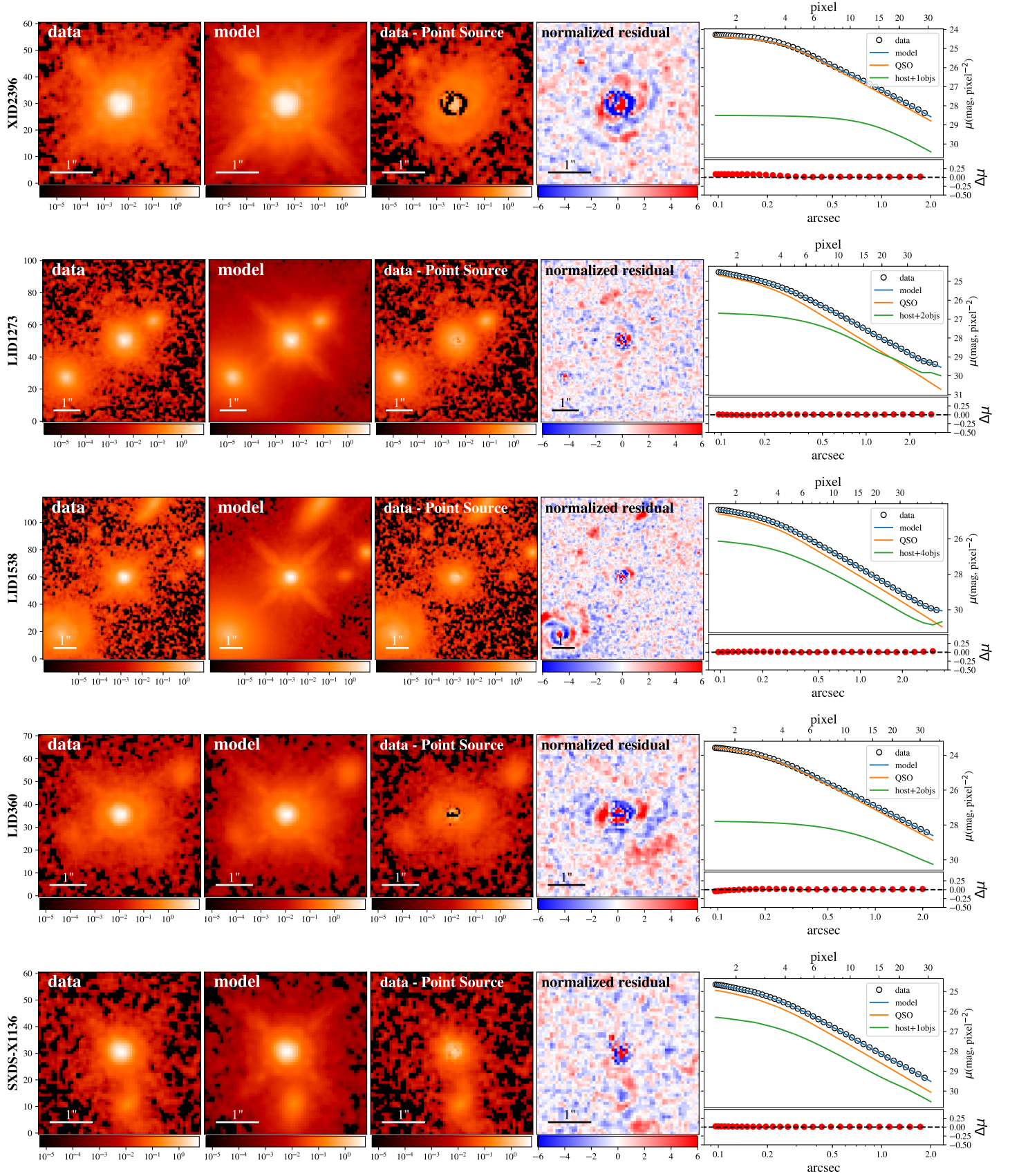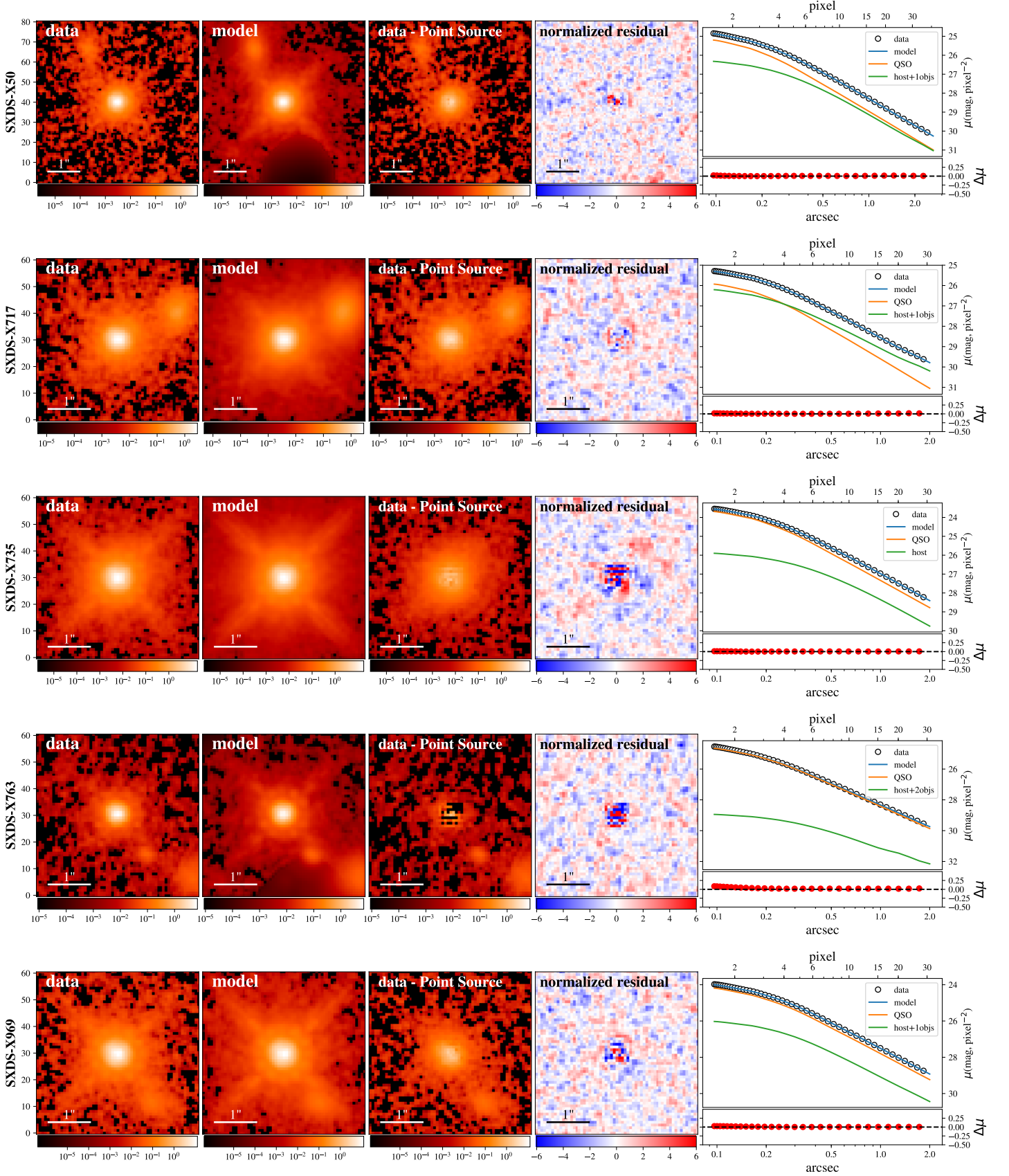
F<small>IG</small>. 1.— Continued.

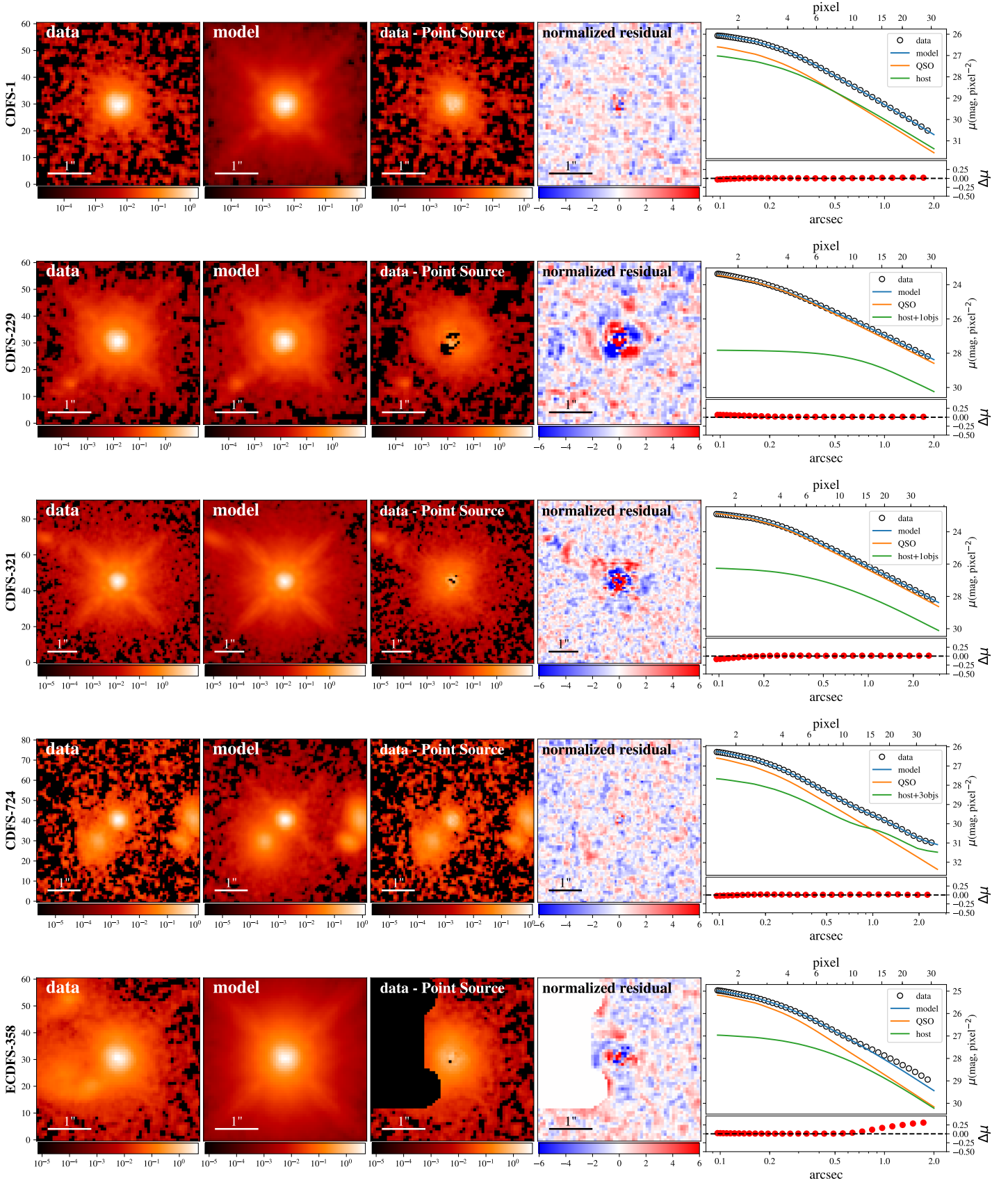FIG. 1.— Continued.

FIG. 1.— Continued.

FIG. 1.— Continued.

FIG. 1.— Continued.